Accepted Manuscript

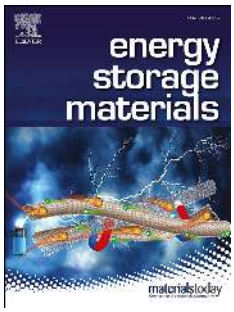

MXene-conducting polymer electrochromic microsupercapacitors

Jianmin Li, Ariana Levitt, Narendra Kurra, Kevin Juan, Natalia Noriega, Xu Xiao, Xuehang Wang, Hongzhi Wang, Husam N. Alshareef, Yury Gogotsi

PII: S2405-8297(19)30495-7

DOI: https://doi.org/10.1016/j.ensm.2019.04.028

Reference: ENSM 723

To appear in: *Energy Storage Materials*

Received Date: 1 April 2019

Accepted Date: 23 April 2019

Please cite this article as: J. Li, A. Levitt, N. Kurra, K. Juan, N. Noriega, X. Xiao, X. Wang, H. Wang, H.N. Alshareef, Y. Gogotsi, MXene-conducting polymer electrochromic microsupercapacitors, *Energy Storage Materials* (2019), doi: https://doi.org/10.1016/j.ensm.2019.04.028.

MXene-Conducting Polymer Electrochromic Microsupercapacitors

Jianmin Li[a,b], *Ariana Levitt*[a], *Narendra Kurra* [a], *Kevin Juan*[a], *Natalia Noriega*[a], *Xu Xiao*[a], *Xuehang Wang* [a], *Hongzhi Wang* [b], *Husam N. Alshareef*[c] *and Yury Gogotsi* [a] *

[a]A.J. Drexel Nanomaterials Institute and Department of Materials Science and Engineering, Drexel University, Philadelphia, PA 19104, USA

[b]State Key Laboratory for Modification of Chemical Fibers and Polymer Materials, College of Materials Science and Engineering, Donghua University, Shanghai 201620, PR China

[c]Department of Materials Science and Engineering, King Abdullah University of Science and Technology (KAUST), Thuwal, 23955-9600, Kingdom of Saudi Arabia.

* *Corresponding author. E-mail: gogotsi@drexel.edu*

Acknowledgements

Authors acknowledge the Core Research Facilities (CRF) at Drexel University for providing access to characterization tools. J. L. acknowledges support through the Fundamental Research Funds for the Central Universities (CUSF-DH-D-2017028) and the Special Excellent Ph.D. International Visit Program by Donghua University. K. J. thanks Prof. Leslie Lamberson and Steve Pagano for organizing the IExE REU at Drexel. A. L. was supported by the National Science Foundation Graduate Research Fellowship under Grant No. DGE-1646737. Research reported in this publication was supported by King Abdullah University of Science and Technology (KAUST) under the KAUST-Drexel Competitive Research Grant (URF/1/2963-01-01).

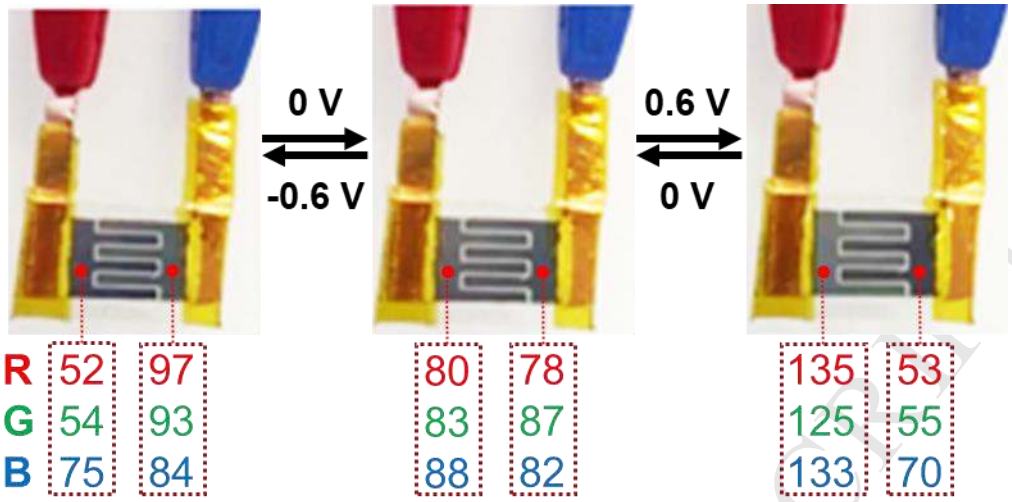

MXene-Conducting Polymer Electrochromic Microsupercapacitors

Abstract

Solution processable two-dimensional transition metal carbides, commonly known as MXenes, have drawn much interest due to their diverse optoelectronic, electrochemical and other useful properties. These properties have been exploited to develop thin and optically transparent microsupercapacitors. However, color changing MXene-based microsupercapacitors have not been explored. In this study, we developed titanium carbide--poly(3,4-ethylenedioxythiophene) (PEDOT) heterostructures by electrochemical deposition using a non-aqueous monomeric electrolytic bath. Planar electrodes of such hybrid films were carved directly using an automated scalpel technique. Hybrid microsupercapacitors showed five-fold areal capacitance and higher rate capabilities (2.4 mF cm^{-2} at 10 mV s^{-1}, retaining 1.4 mF cm^{-2} at 1000 mV s^{-1}) over the pristine MXene microsupercapacitors (455 µF cm^{-2} at 10 mV s^{-1}, 120 µF cm^{-2} at 1000 mV s^{-1}). Furthermore, the electrochromic behavior of PEDOT/$Ti_3C_2T_x$ microsupercapacitors was investigated using *in-situ* UV-vis and resonant Raman spectroscopies. A high-rate color switch between a deep blue and colorless state is achieved on both electrodes in the voltage range of -0.6 to 0.6 V, with switching times of 6.4 and 5.5 s for bleaching and coloration, respectively. This study opens new avenues for developing electrochromic energy storage devices based on MXene heterostructures.

Keywords: MXene, conducting polymer, electrochromic, on-chip, energy storage

1. Introduction

Electrochromic energy storage is rapidly evolving due to its applicability in many technologies including wearable smart textiles [1, 2], bifunctional supercapacitors [3-6], and miniaturized indicators [7, 8]. Combining the advantages of energy storage *via* electrochemical reactions with concomitant color change provides visual indication for charge/discharge states in an electrochromic energy storage device. Two important parameters that affect the performance of electrochemical energy storage devices are the electrode configuration and the electrical conductivity of the charge storing electrode materials. A planar configuration of electrodes in energy storage devices is preferred for easy and compatible integration into small-scale electronic devices and sensors [9-11]. Additionally, this configuration often results in better rate capabilities due to facile diffusion of ions in the planar configuration over sandwich counterparts that employ physical separators [12-14]. In addition to the electrode geometry, the kinetics of electrochromic devices is primarily dependent on the intrinsic electronic/ionic conductivity of the electrode materials [7]. Therefore, planar fabrication of electrochromic electrodes is of significant interest towards the design of high-rate energy storage devices [15]. Though conventional transparent conducting electrodes (TCEs) work well with non-aqueous electrolyte media, such as Indium doped tin oxide (ITO), metal nanowire networks and metallic meshes; multi-step patterning protocols and acidic electrolyte incompatibilities remain major hurdles for developing aqueous on-chip electrochromic energy storage devices [16].

Solution processable conductive two-dimensional (2D) nanomaterials, termed MXenes, are attractive candidates for TCEs as they are hydrophilic, enabling ease of formation of transparent thin films on a variety of substrate platforms [17-19]. Key features of MXenes that are relevant

to TCEs include optical transparency in thin films and excellent electrical conductivity [18]. Further, the redox active metal-oxide like surface and conductive carbide core of MXenes are responsible for their excellent ultra-high rate charge storage capability, especially in acidic electrolytes [20-22]. High quality MXene flakes (1-2 µm) obtained through minimally intensive layer delamination (MILD) method showed electrical figure of merit up to 14 [18]. Diverse physicochemical properties of MXenes enable a multitude of properties including transparency in the visible wavelength range, electronic conductivity and energy storage capabilities – key for transparent energy storage applications. Recently, transparent MXene-based microsupercapacitors have been demonstrated with excellent capacitive storage [18, 19]. Previous work characterized the optoelectronic properties of MXene thin films using ultraviolet-visible (UV-vis) spectroscopy and correlated this data with the electrical conductivity of the films [17].

Poly(3,4-ethylenedixoythiophene) (PEDOT), an electrochromic conducting polymer, shows remarkable chemical and electrochemical stability and exhibits transparency in the doped state, which is suitable for single color changing electrochromic devices [23, 24]. However, $Ti_3C_2T_x$ MXene is electrochemically stable only at cathodic potentials (<0.2 V (vs. Ag/AgCl)), which is a limitation for electrochemical deposition of conducting polymers at anodic potentials (>0.8 V vs. Ag/AgCl) [21, 25]. The combination of those material has demonstrated a remarkably fast electrochemical charge/discharge rate[26].

In this work, acetonitrile was employed as the solvent to exclude the anodic oxidation of MXene during depositing PEDOT on MXene thin films. An automated scalpel lithography was used for direct fabrication of co-planar electrochromic microsupercapacitors (MSC) in a mask-less and resist-free manner [18]. Simultaneous electrochemical storage and electrochromic

functions of PEDOT/$Ti_3C_2T_x$ MSC were demonstrated at a high scan rate of 5000 mV/s. Furthermore, *in-situ* UV-vis and resonant Raman spectroscopies were employed to probe the mechanism of electrochromic behavior of PEDOT/$Ti_3C_2T_x$ heterostructures. This study opens new avenues for developing MXene-based heterostructures for electrochromic energy storage devices.

2. Material and methods

2.1 Synthesis of $Ti_3C_2T_x$ MXene

All chemical reagents were used as received without further purification. Layered ternary carbide Ti_3AlC_2 (MAX phase) powder was obtained from Carbon-Ukraine, Ukraine (particle size < 40 µm). Ti_3C_2 MXene was synthesized by etching Ti_3AlC_2 in a solution produced by adding lithium fluoride (LiF) salt to hydrochloric acid (HCl) solution [26]. The etching solution was prepared by adding 1 g of LiF (Alfa Aesar, 98+ %) to 20 ml of 9 M HCl (Fisher, technical grade, 35-38%), followed by stirring for 5 minutes. 1 g of Ti_3AlC_2 powder was slowly added over the course of a few minutes to the above etchant at room temperature and the solution was stirred continuously for 24 h. The resulting acidic suspension of $Ti_3C_2T_x$ was washed with deionized (DI) water until it reached pH ~ 6 through centrifugation at 3500 rpm (5 min. per cycle) and decanting the supernatant after each cycle. Around pH ~ 6, a stable dark supernatant of $Ti_3C_2T_x$ was observed and collected after 30 minutes of centrifugation at 3500 rpm. The concentration of $Ti_3C_2T_x$ solution was measured by filtering a specific volume of colloidal dispersion through a polypropylene filter (3501 Coated PP, Celgard LLC, Charlotte, NC), followed by overnight drying under vacuum and dividing the dried film's weight over the volume of the colloidal dispersion.

2.2 Spray coating of MXene films

Glass substrates (Fisher Scientific) were cleaned with a soap solution to remove any grease followed by ultrasonication in deionized water and ethanol sequentially for 15 minutes each and then dried by blowing compressed air. The cleaned glass substrates were then plasma cleaned (Tergeo Plus, Pie Scientific) at 50 W with a mixture of O_2/Ar at 3 and 5 sccm for 5 minutes to make the surface hydrophilic. These glass substrates were then spray coated with MXene using a MXene dispersion with a concentration of 2 mg/mL. The spraying time varied to produce films with thicknesses ranging from 20-70 nm. Thin films were finally kept in a desiccator overnight before characterization.

2.3 Electrochemical deposition of poly(3,4-ethylenedioxythiophene)

To prepare the solution for electrodeposition, 100 µL of 3,4-Ethylenedioxythiophene (EDOT, 97%, Sigma-Aldrich) was added into 50 mL of 0.1 M $LiClO_4$/acetonitrile solution. Then, the as-prepared $Ti_3C_2T_x$-coated glass slide was immersed into the above solution and a graphite rod was used as a counter electrode and silver wire as a reference electrode. A constant potential of 1.1 V was applied by a Bio-logic VMP3 workstation. The as-prepared PEDOT/$Ti_3C_2T_x$ semi-transparent electrode was carefully washed by acetonitrile to remove the extra EDOT and $LiClO_4$, followed by drying in a vacuum oven under 60 ℃ for 6 h.

2.4 Fabrication of electrochromic microsupercapacitors

AxiDraw (IJ Instruments Ltd.), and its associated extension in Inkscape 0.91, was used as an automatic X-Y control stage for fabricating MXene microsupercapacitors. Commercially available scalpels (local store, Philadelphia) were loaded onto the slot of an AxiDraw to engrave square wave patterns resulting in interdigitated semi-transparent MXene patterns.

2.5 Preparation of PVA/H_2SO_4 gel electrolyte

1 g of polyvinyl alcohol (PVA) (Alfa Aesar, 98%) was dissolved in 10 mL DI H_2O at 90 °C for 1 h after which the transparent gel was obtained. 1 g (0.6 mL) of concentrated sulfuric acid (Alfa Aesar) was added to 10 wt.% PVA gel and stirred for 30 min to obtain 1 M PVA/H_2SO_4.

2.6 Material Characterization

UV-vis measurements (Evolution 201 UV-vis spectrophotometer, Thermo-Fischer scientific) were performed on different MXene and PEDOT/MXene films to study the optical properties. Cross-sectional images of $Ti_3C_2T_x$ and PEDOT/$Ti_3C_2T_x$ coatings were taken using a scanning electron microscope (SEM) (Zeiss Supra 50VP, Germany). X-ray diffraction (XRD) patterns were measured by a powder diffractometer (Rigaku Smart Lab, USA) with Cu K_α radiation at a step size of 0.04° with 0.5 s dwelling time. Raman spectra were recorded using a Renishaw Raman microscope with LEICA CTR6000 setup with 514 nm laser, 1800 lines mm^{-1} grating at 10% of maximum intensity and 50x objective. Spectra were collected with a dwell time of 120 s and accumulations of 2-4. The electrical conductivities of $Ti_3C_2T_x$ and PEDOT/ $Ti_3C_2T_x$ thin films were measured using a four-point probe (ResTest v1, Jandel Engineering Ltd., Bedfordshire, UK) with a probe distance of 1 mm.

2.7 Electrochemical measurements

The electrochemical tests (cyclic voltammetry (CV), galvanostatic charge-discharge (CD), electrochemical cycling stability) were conducted at room temperature using a VMP3 electrochemical workstation (Bio-Logic, France).

2.8 In-situ UV-visible measurements

Clean glass slides were used for 100% transmittance background correction. The transmittance was recorded from 300 to 1000 nm with 1 nm resolution using deuterium and tungsten lamps. *In-situ* UV-vis spectra were conducted by combining the UV–vis spectrometer with a BioLogic SP

150 potentiostat. The UV-vis spectra under different voltages were recorded while running cyclic voltammetry (CV) at 10 mV s^{-1}.

2.9 In-situ Raman measurements

A two-electrode open system was used for the *in-situ* Raman spectroscopy measurements. The as-prepared PEDOT/$Ti_3C_2T_x$ MSC was connected to a BioLogic SP 150 potentiostat and placed on the test stage. The laser was focused on one of the electrodes. The Raman spectra at different voltages were recorded during the CV scan at a scan rate of 10 mV s^{-1}.

2.10 2-electrode configuration (device measurements)

Areal capacitance was calculated using equation (1):

$$C_A = \frac{1}{VAv}\int idV \quad (1)$$

where *i* is the current (mA), *V* is the voltage window of the device (V), v is the scan rate (mV/s), *A* is the geometrical footprint area of the device including total area of finger electrodes and interspace regions. $\int idV$ is the integrated area over the discharge portion of the correpsoding CV scan.

Volumetric and areal energy and power densities were calculated using equations (2) and (3):

$$\text{Energy density, } E_V = \frac{1}{\Gamma}\int iVdt \quad (2)$$

$$\text{Power density, } P_V = \frac{E_V}{\Delta t} \quad (3)$$

Where Γ is the area or volume of the device and Δt is the discharge time (s).

3. Results and Discussions

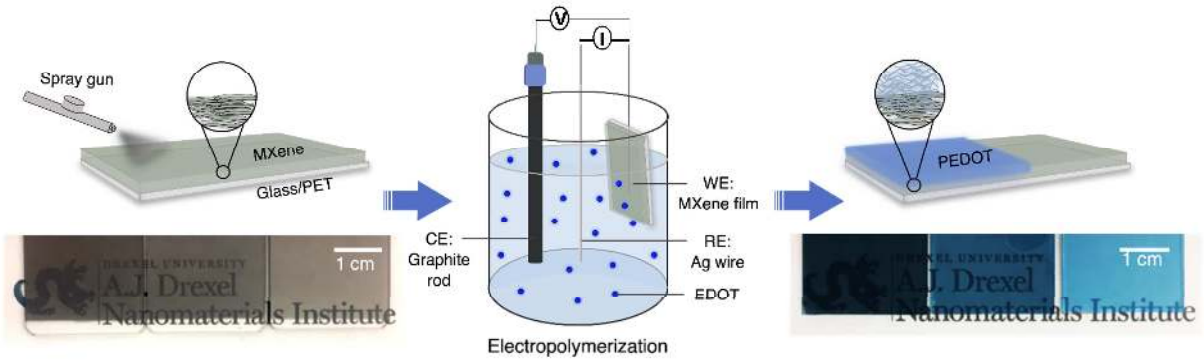

Figure 1. Schematic depicting the formation process for hybrid PEDOT/$Ti_3C_2T_x$ films. Spray coated $Ti_3C_2T_x$ films on glass substrates. Electrochemical polymerization of poly(3,4-ethylenedioxythiophene), PEDOT on MXene thin films. Corresponding digital photographs of $Ti_3C_2T_x$ (left) and PEDOT/$Ti_3C_2T_x$ (right) thin films are shown.

The schematic shown in **Figure 1** illustrates the process of depositing $Ti_3C_2T_x$/PEDOT thin films onto glass substrates. For spray coating, $Ti_3C_2T_x$ was synthesized through the minimally intensive layer delamination (MILD) method as reported previously [27], and a colloidal solution of $Ti_3C_2T_x$ in water was collected. It was demonstrated that pre-intercalated hydrated Li-ions assist in delaminating MXene flakes through manual shaking. The colloidal stability of such MXene dispersions is attributed to its negative zeta potentials, originating from surface functional groups (T_x: -OH, -O, -F, -Cl). During the spray coating process, instantaneous drying causes evaporation of water, producing restacked MXene flakes as a continuous thin film. It is possible to control the thickness of MXene films by adjusting the concentration of the MXene dispersion and the spraying duration. Typical sheet resistance values of MXene films vary from

20 to 100 Ω/sq for the thicknesses ranging from 70 to 20 nm. The as-prepared MXene thin films have transmittance values varying from 80% to 54% when the thickness varies from 20 to 40 nm.

Considering its transmittance and conductivity together, spray-coated MXene thin films with a thickness of about 40 nm and transmittance of 54% at 550 nm were used as TCEs for depositing PEDOT. MXene serves as a TCE due to its ability to be electrically conductive while being optically transparent. It is important to note that aqueous electrolytic baths were not viable for the electrochemical deposition of PEDOT onto MXene films because the required anodic potentials cause irreversible oxidation of MXene (**Figure S1**, **Supplementary Information**). As such, a non-aqueous electrolytic bath (EDOT + 0.1 M $LiClO_4$ + acetonitrile) was used to avoid the oxidation of MXene at anodic potentials while depositing PEDOT. The corresponding digital photographs of $Ti_3C_2T_x$ and PEDOT/$Ti_3C_2T_x$ thin films were shown in **Figure 1** and the UV-vis spectra were shown in **Figure S2**.

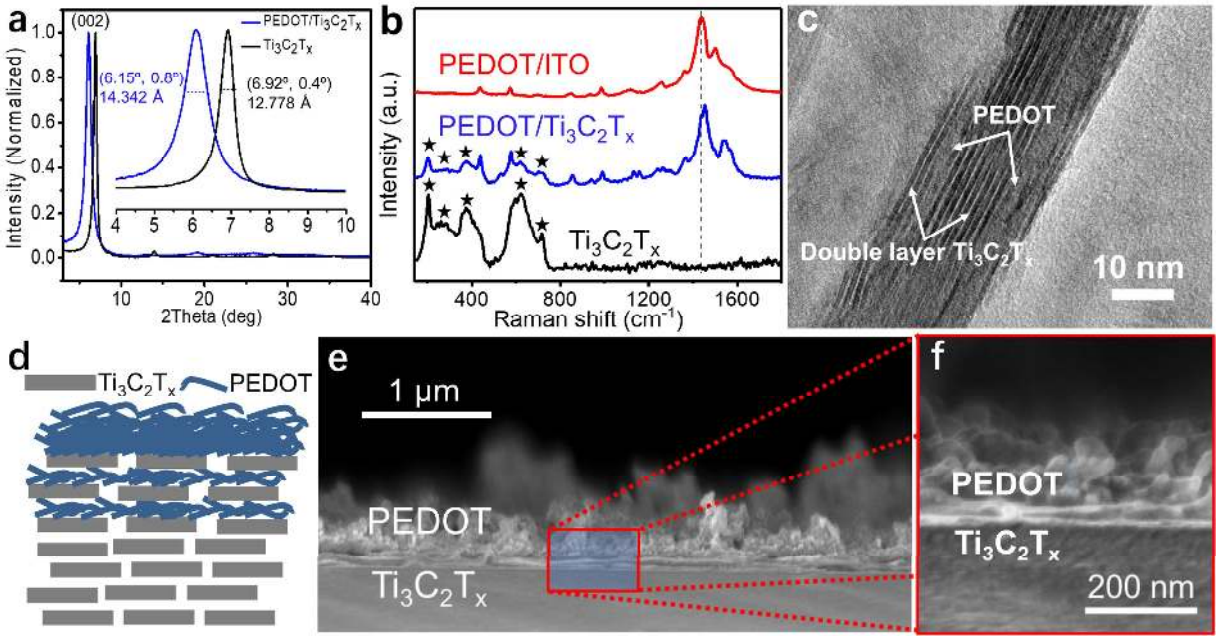

Figure 2. (a) X-ray diffraction (XRD) patterns of PEDOT/$Ti_3C_2T_x$ and pristine $Ti_3C_2T_x$ thin films, inset shows (002) peak shift after electrodeposition of PEDOT (b) Raman spectra of PEDOT/ITO, PEDOT/$Ti_3C_2T_x$, and pristine $Ti_3C_2T_x$. Stars are indicative of $Ti_3C_2T_x$ signature peaks. (c) High-resolution cross-section TEM image of the PEDOT/$Ti_3C_2T_x$ film, (d) schematic illustrating nucleation and growth of PEDOT on the surface and in top few $Ti_3C_2T_x$ layers. (e)

Cross-sectional scanning electron microscopy (SEM) image of PEDOT deposited on $Ti_3C_2T_x$, (f) magnified view of PEDOT/$Ti_3C_2T_x$ interface.

The structural aspects of PEDOT/$Ti_3C_2T_x$ and $Ti_3C_2T_x$ were investigated using X-ray diffraction (XRD). The (002) peak of $Ti_3C_2T_x$ was prominent after the electrochemical deposition of PEDOT, signifying that the alignment of MXene layers was preserved (**Figure 2**a). However, a shift towards lower 2Θ was observed for PEDOT/$Ti_3C_2T_x$ compared to $Ti_3C_2T_x$. The apparent increase in the *d*-spacing up to 16 Å with nearly double the full width at half maximum (FWHM) of the (002) peak was observed for PEDOT/$Ti_3C_2T_x$ with respect to pristine $Ti_3C_2T_x$. Based on our previous work, polar solvents such as acetonitrile and propylene carbonate may intercalate spontaneously between the MXene layers [28]. This could lead to penetration of solvated EDOT monomers into the top layers of MXene flakes. Such kind of expansion of MXene layers is beneficial for better accommodation and faster transport of ions between otherwise re-stacked MXene layers. Based on Raman spectra, the chemical nature of PEDOT grown on both MXene and ITO surfaces through electrochemical deposition remains the same, as shown in **Figure 2**b. The most intense peak at 1439 cm^{-1} is due to the symmetric stretching of C_α=C_β which provides information about the level of oxidation of PEDOT. The bands at 1514 cm^{-1} is due to asymmetric C_α=C_β stretching; 1359 cm^{-1} corresponds to C_β–C_β inter-ring stretching, 1257 cm^{-1} represents C_α–C_α inter-ring stretching, 1116 cm^{-1} is due to C-O-C deformation, 982 cm^{-1} represents C-C anti-symmetrical stretching mode, 700 cm^{-1} corresponds to symmetric C-S-C deformation, 571 cm^{-1} due to oxy-ethylene ring deformation [29, 30]. In the case of PEDOT/$Ti_3C_2T_x$, C_α=C_β stretching peak shifts to higher wavenumber, possibly due to electrostatic attachment of the negatively charged MXene surface with the PEDOT moieties. The PEDOT intercalated fibers between MXene layers was further confirmed by high-resolution

transmission electron microscopy (HRTEM) (**Figure 2**c), from which some of the confined PEDOT chains between MXene layers can be visualized. The schematic shown in **Figure 2**d illustrates the PEDOT/MXene heterostructure where the intimate coupling between top MXene layers and PEDOT chains is beneficial for synergistic improvement in electrochemical performance. The morphology of PEDOT is seen as small fibroid-type particles glued to the MXene surface (shown in **Figure 2**e). The thickness of the PEDOT layer was approximately 70 - 100 nm, depending on the deposition duration. As shown in **Figure 2**f, dense deposition of PEDOT on top of the MXene surface and the overall conductivity of PEDOT/$Ti_3C_2T_x$ are also influenced by the intrinsic electrical conductivity of PEDOT deposited during this process.

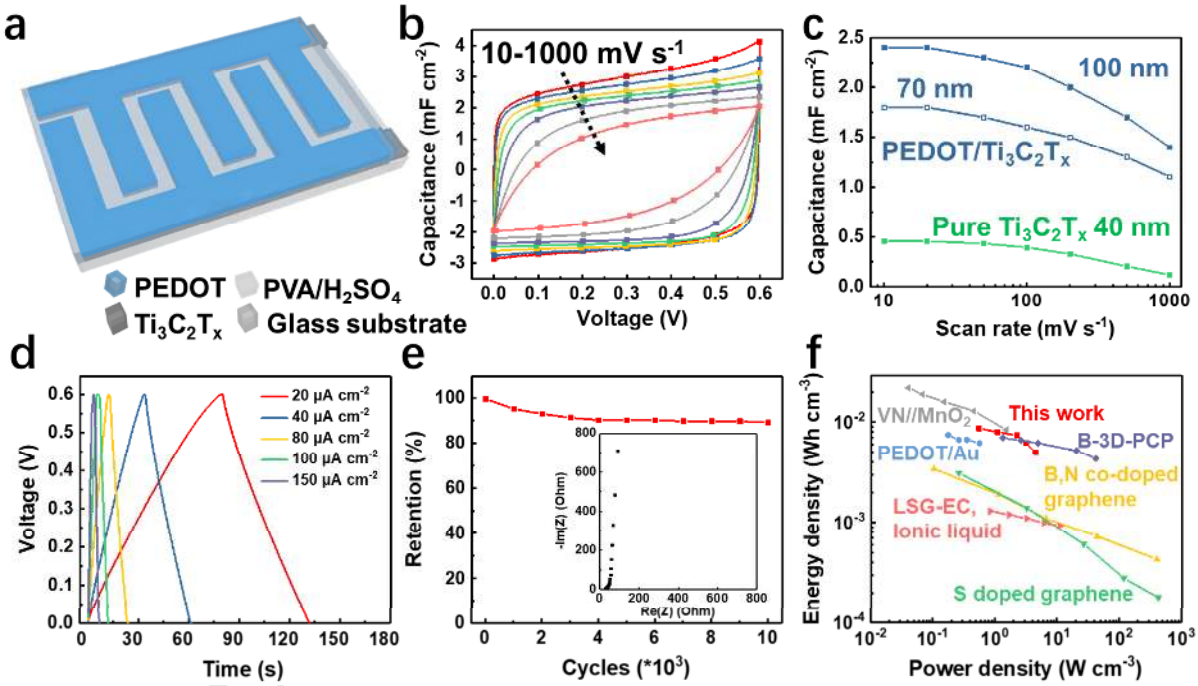

Figure 3. (a) Schematic of PEDOT/$Ti_3C_2T_x$ symmetric microsupercapacitor (MSC), (b) cyclic voltammograms at different scan rates, (c) variation of areal capacitance with scan rate, (d) galvanostatic charge discharge curves at different current densities, (e) cycling stability of PEDOT/$Ti_3C_2T_x$ MSC for 10000 cycles at a scan rate of 100 mV/s, the inset shows Nyquist plot of the device and (f) Ragone plot of (100 nm) PEDOT/$Ti_3C_2T_x$ MSC compared with the reported MSCs[31-36].

The schematic in **Figure 3**a shows the PEDOT/$Ti_3C_2T_x$ microsupercapacitor (MSC) device configuration. The pattern was fabricated by the automated scalpel engraving technique as described previously [18]. Due to the superior electronic conductivity of MXene compared to PEDOT, the PEDOT is presumed to primarily contribute to the charge storage while MXene serves as a current collecting layer. Pure 40-nm MXene films studied in this work had conductivity of ~2500 S/cm, while the PEDOT-MXene film of 100 nm thickness had the conductivity of ~1000 S/cm. During the charging process, the positive PEDOT electrode was doped by SO_4^{-2} or bisulfate ions, while the protons intercalated into the negatively polarized PEDOT electrodes [37, 38]. Anion doping causes the oxidation of PEDOT while cation doping causes the reduction of PEDOT. Doped PEDOT is more conductive than undoped PEDOT and accordingly a color contrast is observed between the fingers [37]. To evaluate electrochemical performance, cyclic voltammetry (CV) and galvanostatic charge-discharge (GCD) measurements were conducted. **Figure 3**b shows the typical CV curves of (100 nm) PEDOT/ $Ti_3C_2T_x$ MSC in the voltage window of 0-0.6 V at various scan rates from 10 to 1000 mV s^{-1}. The rectangular shape was maintained even at a scan rate of 1000 mV s^{-1} due to fast redox reactions related to doping/dedoping processes at the surface of the conducting polymer electrodes. On the contrary, the CV curves of pristine $Ti_3C_2T_x$ and 70 nm PEDOT/$Ti_3C_2T_x$ MSC, shown in **Figure S3**, exhibit a much lower capacitance compared to 100 nm PEDOT/$Ti_3C_2T_x$ MSC. As expected, capacitive performance of the device was improved by increasing the deposition of PEDOT. It is important to note that compared to the previously reported electrochromic MSCs employing metal current collectors, our PEDOT/$Ti_3C_2T_x$ MSC exhibited quite rectangular CV curves [9, 11], signifying the good ohmic coupling between PEDOT and $Ti_3C_2T_x$. As shown in **Figure 3**c, the areal capacitance of the PEDOT/$Ti_3C_2T_x$ and pristine $Ti_3C_2T_x$ MSCs were compared. Notably,

for the 100 nm device, a high capacitance of 2.4 mF cm^{-2} was achieved at 10 mV s^{-1}, retaining 58% (1.4 mF cm^{-2}) at a scan rate of 1000 mV s^{-1}, while for pristine $Ti_3C_2T_x$ device is 455 µF cm^{-2} at 10 mV s^{-1}, with a 26% retention (120 µF cm^{-2}) at 1000 mV s^{-1}. Moreover, for the 70 nm device, capacitance of 1.8 mF cm^{-2} at 10 mV s^{-1} was observed, retaining 61% (1.1 mF cm^{-2}) at 1000 mV s^{-1}. Such a high-rate performance could be attributed to the high ionic conductivity of the heterostructure of metallic $Ti_3C_2T_x$ and conducting PEDOT and the enlarged interlayer space of $Ti_3C_2T_x$ by the intercalation of PEDOT.

The GCD curves of the (100 nm) PEDOT/$Ti_3C_2T_x$ MSC at different current densities are shown in **Figure 3**d. Furthermore, we evaluated its electrochemical cycling stability by repeating CVs for 10,000 times at 100 mV s^{-1}. As shown in **Figure 3**e, 90% of the capacitance was retained after 10,000 cycles at a Coulombic efficiency of 100%. The inset of **Figure 3**e shows a Nyquist plot for the PEDOT/$Ti_3C_2T_x$ MSC, from which the vertical line in the low-frequency region is an indication of typical capacitive behavior. A low interfacial resistance was evident, as there is no semi-circle in the high frequency region. The Ragone plot, shown in **Figure 3**f, demonstrates the energy and power density of the 100 nm PEDOT/$Ti_3C_2T_x$ MSC. Notably the 100 nm PEDOT/$Ti_3C_2T_x$ MSC delivered a specific volumetric energy density of up to 8.7 mWh cm^{-3} at a power density of 0.55 W cm^{-3}, also providing high power density of 4.5 W cm^{-3} at 5.0 mWh cm^{-3}, which is superior to activated carbon and graphene-based MSCs [31-34]. Furthermore, these results are superior to many pseudocapacitive microsupercapacitors, including the VN//mesoporous MnO_2 MSC [35], and the PEDOT/Au MSC [36]. Our 100 nm PEDOT/$Ti_3C_2T_x$ MSC showed an order of magnitude enhancement compared to the previously reported PEDOT/Au MSC at similar thickness [36], which can be attributed to the high conductivity of the PEDOT/$Ti_3C_2T_x$ composite, the expanded interspace of $Ti_3C_2T_x$ layers during

the deposition of PEDOT and additional charge storage contribution from bottom MXene TCE layer as well.

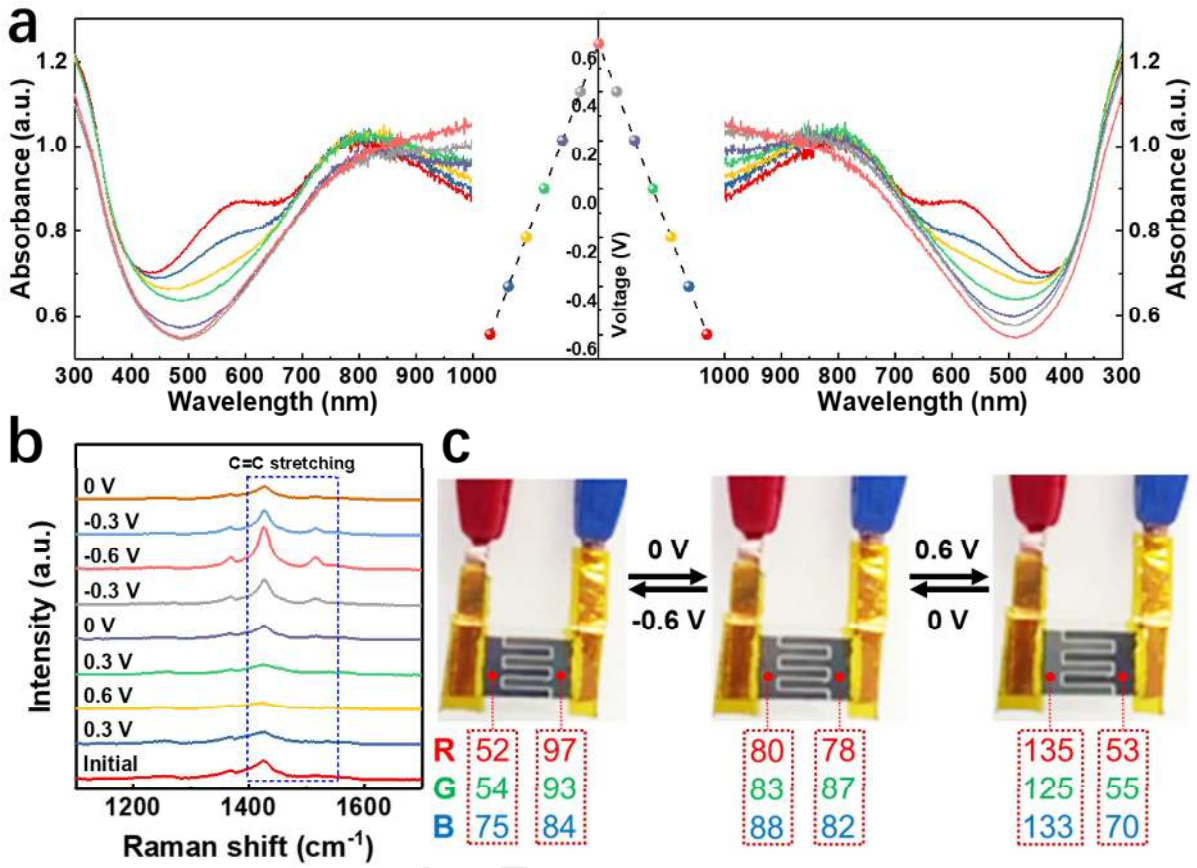

Figure 4. *In-situ* spectra recorded on 100 nm PEDOT/$Ti_3C_2T_x$ finger electrodes. (a) *In-situ* UV-vis spectra at different voltages during the CV test. (b) *In-situ* resonant Raman spectra of the PEDOT/$Ti_3C_2T_x$ electrode during the CV scan. (c) Digital images at different voltages showing the color changes of the finger electrodes in reversible manner and the corresponding RGB values are shown.

To demonstrate the electrochromic effect of the as-prepared electrochromic on-chip 100 nm PEDOT/$Ti_3C_2T_x$ symmetric MSC, an *in-situ* UV-vis spectro-electrochemical technique was employed to monitor the transmittance changes between 300-1000 nm in response to the CV scan between -0.6 and 0.6 V (at a scan rate of 10 mV s^{-1}). As shown in **Figure 4**a, during the charging process from 0 to 0.6 V, the color of the PEDOT/$Ti_3C_2T_x$ positive electrode gradually

became lighter and the absorption at 488 nm decreased, corresponding to the doping of SO_4^{2-} ions. When the voltage reached 0.6 V, the lighter color and the higher transmittance over the pristine electrode was observed. During the charging process from 0 to -0.6 V, corresponding to the proton doping behavior, the color of the PEDOT/$Ti_3C_2T_x$ got deeper and the absorption between 400 to 700nm increased. Notably, a new peak was observed at 589 nm as the voltage increased, which should be influenced by $Ti_3C_2T_x$, which retained its absorption peak during the electrochemical process. The UV-vis spectra during the discharge process from 0.6 to 0 V and from -0.6 to 0 V verified the reversibility of the color change. UV-vis spectra of the pristine $Ti_3C_2T_x$ device were recorded at different voltages to confirm the contribution of PEDOT to the electrochromic behavior, as shown in **Figure S4**. Though relatively high electrochromic activity was observed on pure $Ti_3C_2T_x$ in a 3-electrode cell [39], only a slight difference could be observed with the change in voltage for the pristine symmetric MXene MSC. From this, we conclude that the main role of $Ti_3C_2T_x$ is to provide high electronic conductivity while PEDOT primarily contributes to the charge storage and electrochromic behavior. Digital images of the PEDOT/$Ti_3C_2T_x$ device at different voltages, shown in **Figure 4**c, agree with the UV-vis spectra. The RGB values of each electrode at different status were calculated and shown below these images.

Raman spectroscopy allowed for a detailed and time-resolved investigation of the kinetics of complex physical or chemical processes in a nondestructive manner. We employed a 514 nm laser excitation to exploit the resonant Raman phenomenon of PEDOT during electrochemical oxidation and reduction. **Figure 4**b shows the voltage-dependent changes for the Raman bands of PEDOT when the device was scanned between -0.6 and 0.6 V at a scan rate of 10 mV s^{-1}, meaning that the evolution in Raman bands is reversible. The main peak at 1425 cm^{-1} is

broadened and shifted to 1445 cm^{-1} due to electrochemical doping process [40]. During the scan from 0 to 0.6 V, the specific Raman peaks of C=C bonds at 1425 and 1514 cm^{-1} indicated a dramatic decrease in intensity. When scanned back from 0.6 to 0 V, the intensities of these peaks are reverted to their original intensities. While these peaks were significantly enhanced, when the device was scanned from 0 to -0.6 V, they decreased back during the scanning from -0.6 to 0 V. To quantify the change of Raman peaks, we calculated the ratio of the intensity of these two peaks related to C=C bond with the peak at 1454 cm^{-1}, since this peak only showed a slight change with applied voltages (see **Table S1**). These results are consistent with the doping-dedoping process of protons and SO_4^{2-}. When charged to a positive potential, the PEDOT was doped by SO_4^{2-} ions to reach its oxidation state. This change may induce the decrease of its polarizability, which is responsible for the decrease of Raman peaks intensity. On the other hand, the doping of protons could increase the polarizability, which resulted in an increase of the Raman peak intensities. In other words, charging to -0.6V caused the PEDOT band gaps to resonate with 514 nm and hence increased intensities of Raman peaks. At voltages of 0 and 0.6V, PEDOT is non-resonant with the laser wavelengths and hence diminished intensities. These results are in agreement with the resonant Raman studies on PEDOT electrodes [40].

Figure S5a reveals the *in-situ* transmittance at 488 nm under a pulse voltage of ±0.6 V because the biggest difference of transmittance was observed at 488 nm. The switching times were calculated to be 6.4 s and 5.5 s for bleaching and coloration, respectively, which is faster than most of the reported electrochromic devices (see **Table S2**). Furthermore, two videos (see **Supplementary Information**) were conducted during the CV test at 10 mV s^{-1} and 5 V s^{-1}, to demonstrate the high switching speeds of PEDOT/$Ti_3C_2T_x$ MSC. As with the high-rate performance, this fast switching speed can be attributed to the high conductivity and the uniform

electric field distribution of the bottom-layer $Ti_3C_2T_x$. In addition, the conducting PEDOT has a much higher conductivity than electrochromic transition metal oxides [23] such as WO_3 [6], NiO [41], and V_2O_5 [42]. The cycle stability of the bleaching-coloration was shown in **Figure S5**b, which was tested by repeating the pulse voltage of **±**0.6 V for 300 cycles. The transmittance of bleached and colored states was stable during the test, indicating a steady color change process.

4. Conclusions

Electrochromic energy storage using a MXene-PEDOT heterostructure has been demonstrated. Direct fabrication of the MXene-PEDOT microsupercapacitors has been achieved through automated scalpel lithography. A high areal capacitance of 2.4 mF cm^{-2} was achieved for the (100 nm) PEDOT/$Ti_3C_2T_x$ MSC at a scan rate of 10 mV s^{-1}, retaining 1.4 mF cm^{-2} at 1000 mV s^{-1}. Moreover, *in-situ* UV-vis and resonant Raman spectroscopies were employed to analyze the electrochromic behavior of PEDOT/$Ti_3C_2T_x$ MSC. Color-switching time of 6.4 s for bleaching and 5.5 s for coloration was obtained. This study opens new avenues for developing MXene-conducting polymer heterostructures for color-changing energy storage devices.

References

[1] X. Chen, H. Lin, J. Deng, Y. Zhang, X. Sun, P. Chen, X. Fang, Z. Zhang, G. Guan, H. Peng, Electrochromic Fiber-Shaped Supercapacitors, Adv. Mater. 26 (2014) 8126-8132.

[2] W. Weng, P. Chen, S. He, X. Sun, H. Peng, Smart Electronic Textiles, Angew. Chem. Int. Ed. 55 (2016) 6140-6169.

[3] H. Li, J. Li, C. Hou, D. Ho, Q. Zhang, Y. Li, H. Wang, Solution-Processed Porous Tungsten Molybdenum Oxide Electrodes for Energy Storage Smart Windows, Adv. Mater. Technol. 2 (2017) 1700047.

[4] S. Lin, X. Bai, H. Wang, H. Wang, J. Song, K. Huang, C. Wang, N. Wang, B. Li, M. Lei, H. Wu, Roll-to-Roll Production of Transparent Silver-Nanofiber-Network Electrodes for Flexible Electrochromic Smart Windows, Adv. Mater. 29 (2017) 1703238.

[5] Z. Liu, H.I. Wang, A. Narita, Q. Chen, Z. Mics, D. Turchinovich, M. Kläui, M. Bonn, K. Müllen, Photoswitchable Micro-Supercapacitor Based on a Diarylethene-Graphene Composite Film, J. Am. Chem. Soc. 139 (2017) 9443-9446.

[6] T.Y. Yun, X. Li, S.H. Kim, H.C. Moon, Dual-Function Electrochromic Supercapacitors Displaying Real-Time Capacity in Color, ACS Appl. Mater. Inter. 10 (2018) 43993-43999.

[7] P. Yang, P. Sun, W. Mai, Electrochromic energy storage devices, Mater. Today 19 (2016) 394-402.

[8] L. Zhang, M. Liao, L. Bao, X. Sun, H. Peng, The Functionalization of Miniature Energy□Storage Devices, Small Methods 1 (2017) 1700211.

[9] S. Qin, Q. Zhang, X. Yang, M. Liu, Q. Sun, Z.L. Wang, Hybrid Piezo/Triboelectric□Driven Self□Charging Electrochromic Supercapacitor Power Package, Adv. Energy Mater. 8 (2018) 1800069.

[10] T.G. Yun, D. Kim, Y.H. Kim, M. Park, S. Hyun, S.M. Han, Photoresponsive Smart Coloration Electrochromic Supercapacitor, Adv. Mater. 29 (2017) 1606728.

[11] P. Zhang, F. Zhu, F. Wang, J. Wang, R. Dong, X. Zhuang, O.G. Schmidt, X. Feng, Stimulus□Responsive Micro□Supercapacitors with Ultrahigh Energy Density and Reversible Electrochromic Window, Adv. Mater. 29 (2017) 1604491.

[12] K. Laszczyk, D. Futaba, K. Kobashi, K. Hata, T. Yamada, A. Sekiguchi, The limitation of electrode shape on the operational speed of a carbon nanotube based micro-supercapacitor, Sustain. Energ. Fuels 1 (2017) 1282-1286.

[13] Y. Shao, J. Li, Y. Li, H. Wang, Q. Zhang, R.B. Kaner, Flexible quasi-solid-state planar micro-supercapacitor based on cellular graphene films, Mater. Horiz. 4 (2017) 1145-1150.

[14] P. Huang, C. Lethien, S. Pinaud, K. Brousse, R. Laloo, V. Turq, M. Respaud, A. Demortiere, B. Daffos, P.L. Taberna, On-chip and freestanding elastic carbon films for micro-supercapacitors, Science 351 (2016) 691-695.

[15] N.A. Kyeremateng, T. Brousse, D. Pech, Microsupercapacitors as miniaturized energy-storage components for on-chip electronics, Nat. Nanotechnol. 12 (2017) 7.

[16] C.J. Zhang, V. Nicolosi, Graphene and MXene-based transparent conductive electrodes and supercapacitors, Energy Storage Mater. 16 (2018) 102-125.

[17] K. Hantanasirisakul, M.Q. Zhao, P. Urbankowski, J. Halim, B. Anasori, S. Kota, C.E. Ren, M.W. Barsoum, Y. Gogotsi, Fabrication of $Ti_3C_2T_x$ MXene transparent thin films with tunable optoelectronic properties, Adv. Electron. Mater. 2 (2016) 1600050.

[18] P. Salles, E. Quain, N. Kurra, A. Sarycheva, Y. Gogotsi, Automated Scalpel Patterning of Solution Processed Thin Films for Fabrication of Transparent MXene Microsupercapacitors, Small 14 (2018) 1802864.

[19] C. Zhang, B. Anasori, A. SeralAscaso, S.H. Park, N. McEvoy, A. Shmeliov, G.S. Duesberg, J.N. Coleman, Y. Gogotsi, V. Nicolosi, Transparent, Flexible, and Conductive 2D Titanium Carbide (MXene) Films with High Volumetric Capacitance, Adv. Mater. 29 (2017) 1702678.

[20] B. Anasori, M.R. Lukatskaya, Y. Gogotsi, 2D metal carbides and nitrides (MXenes) for energy storage, Nat. Rev. Mater. 2 (2017) 16098.

[21] S. Wang, X. Zhao, X. Yan, Z. Xiao, C. Liu, Y. Zhang, X. Yang, Regulating Fast Anionic Redox for High-Voltage Aqueous Hydrogen-Ion-based Energy Storage, Angew. Chem. 131 (2019) 211-216.

[22] Y. Xia, T.S. Mathis, M. Zhao, B. Anasori, A. Dang, Z. Zhou, H. Cho, Y. Gogotsi, S. Yang, Thickness-independent capacitance of vertically aligned liquid-crystalline MXenes, Nature 557 (2018) 409.

[23] A.A. Argun, P.H. Aubert, B.C. Thompson, I. Schwendeman, C.L. Gaupp, J. Hwang, N.J. Pinto, D.B. Tanner, A.G. MacDiarmid, J.R. Reynolds, Multicolored electrochromism in polymers: structures and devices, Chem. Mater. 16 (2004) 4401-4412.

[24] J. Li, H. Li, J. Li, G. Wu, Y. Shao, Y. Li, Q. Zhang, H. Wang, A single-walled carbon nanotubes/poly(3,4-ethylenedioxythiophene)-poly(styrenesulfonate)/copper

hexacyanoferrate hybrid film for high-volumetric performance flexible supercapacitors, J. Power Sources 386 (2018) 96-105.

[25] J. Li, N. Kurra, M. Seredych, X. Meng, H. Wang, Y. Gogotsi, Bipolar carbide-carbon high voltage aqueous lithium-ion capacitors, Nano Energy 56 (2019) 151-159.

[26] G.S. Gund, J.H. Park, R. Harpalsinh, M. Kota, J.H. Shin, T.-i. Kim, Y. Gogotsi, H.S. Park, MXene/Polymer Hybrid Materials for Flexible AC-Filtering Electrochemical Capacitors, Joule 3 (2019) 164-176.

[27] M. Alhabeb, K. Maleski, B. Anasori, P. Lelyukh, L. Clark, S. Sin, Y. Gogotsi, Guidelines for Synthesis and Processing of Two-Dimensional Titanium Carbide ($Ti_3C_2T_x$ MXene), Chem. Mater. 29 (2017) 7633-7644.

[28] X. Wang, T.S. Mathis, K. Li, Z. Lin, L. Vlcek, T. Torita, N.C. Osti, C. Hatter, P. Urbankowski, A. Sarycheva, M. Tyagi, E. Mamontov, P. Simon, Y. Gogotsi, Influences from solvents on charge storage in titanium carbide MXenes, Nat. Energy 4 (2019) 241-248.

[29] P. Subramanian, N. Clark, B. WintherJensen, D. MacFarlane, L. Spiccia, Vapour-phase polymerization of pyrrole and 3, 4-ethylenedioxythiophene using iron (III) 2, 4, 6-trimethylbenzenesulfonate, Aust. J. Chem. 62 (2009) 133-139.

[30] B. Winther-Jensen, K. West, Vapor-phase polymerization of 3, 4-ethylenedioxythiophene: a route to highly conducting polymer surface layers, Macromolecules 37 (2004) 4538-4543.

[31] Z. Wu, K. Parvez, A. Winter, H. Vieker, X. Liu, S. Han, A. Turchanin, X. Feng, K. Müllen, Layer-by-Layer Assembled Heteroatom-Doped Graphene Films with Ultrahigh

Volumetric Capacitance and Rate Capability for Micro-Supercapacitors, Adv. Mater. 26 (2014) 4552-4558.

[32] Z. Wu, Y. Tan, S. Zheng, S. Wang, K. Parvez, J. Qin, X. Shi, C. Sun, X. Bao, X. Feng, K. Müllen, Bottom-Up Fabrication of Sulfur-Doped Graphene Films Derived from Sulfur-Annulated Nanographene for Ultrahigh Volumetric Capacitance Micro-Supercapacitors, J. Am. Chem. Soc. 139 (2017) 4506-4512.

[33] C. Kim, D.Y. Kang, J.H. Moon, Full lithographic fabrication of boron-doped 3D porous carbon patterns for high volumetric energy density microsupercapacitors, Nano Energy 53 (2018) 182-188.

[34] M.F. ElKady, V. Strong, S. Dubin, R.B. Kaner, Laser Scribing of High-Performance and Flexible Graphene-Based Electrochemical Capacitors, Science 335 (2012) 1326-1330.

[35] J. Qin, S. Wang, F. Zhou, P. Das, S. Zheng, C. Sun, X. Bao, Z. Wu, 2D mesoporous MnO_2 nanosheets for high-energy asymmetric micro-supercapacitors in water-in-salt gel electrolyte, Energy Storage Mater. 18 (2018) 393-404.

[36] N. Kurra, M.K. Hota, H.N. Alshareef, Conducting polymer micro-supercapacitors for flexible energy storage and AC line-filtering, Nano Energy 13 (2015) 500-508.

[37] G. Cai, P. Darmawan, M. Cui, J. Wang, J. Chen, S. Magdassi, P.S. Lee, Highly Stable Transparent Conductive Silver Grid/PEDOT:PSS Electrodes for Integrated Bifunctional Flexible Electrochromic Supercapacitors, Adv. Energy Mater. 6 (2016) 1501882.

[38] R. Liu, J. Duay, T. Lane, S. Bok Lee, Synthesis and characterization of RuO_2/poly(3,4-ethylenedioxythiophene) composite nanotubes for supercapacitors, Phys. Chem. Chem. Phys. 12 (2010) 4309-4316.

[39] P. Salles, D. Pinto, K. Hantanasirisakul, K. Maleski, C.E. Shuck, Y. Gogotsi, Electrochromic Effect in Titanium Carbide MXene Thin Films Produced by Dip-Coating, Adv. Funct. Mater. (2019) 1809223.

[40] S. Garreau, G. Louarn, J. Buisson, G. Froyer, S. Lefrant, In situ spectroelectrochemical Raman studies of poly (3, 4-ethylenedioxythiophene)(PEDT), Macromolecules 32 (1999) 6807-6812.

[41] D. Dong, W. Wang, A. Rougier, G. Dong, M. Da Rocha, L. Presmanes, K. Zrikem, G. Song, X. Diao, A. Barnabé, Life-cycling and uncovering cation-trapping evidence of a monolithic inorganic electrochromic device: glass/ITO/WO_3/$LiTaO_3$/NiO/ITO, Nanoscale 10 (2018) 16521-16530.

[42] P. Zhang, F. Zhu, F. Wang, J. Wang, R. Dong, X. Zhuang, O.G. Schmidt, X. Feng, Stimulus-Responsive Micro-Supercapacitors with Ultrahigh Energy Density and Reversible Electrochromic Window, Adv. Mater. 29 (2017) 1604491.